A comparison of the experimental and theoretical charge density distributions in two polymorphic modifications of Piroxicam.

Felcia Lai,[1] Jonathan J. Du,[1] Peter A. Williams,[1,2] Linda Váradi,[1] Daniel Baker,[3] Paul W. Groundwater,[1] Jacob Overgaard,[4] James A. Platts[5] and David E. Hibbs[1]*

[1]*Faculty of Pharmacy, The University of Sydney, NSW 2006 Australia*

[2]*School of Science and Health, Western Sydney University, Locked Bag 1797, Penrith, NSW, 2751*

[3]*Rigaku Oxford Diffraction, Oxford Industrial Park, Yarnton, Oxfordshire, OX5 1QU, UK*

[4]*Department of Chemistry, Center for Materials Crystallography, Aarhus University, Langelandsgade 140, Aarhus C, 8000, Denmark*

[5]*School of Chemistry, Cardiff University, P.O. Box 912, Cardiff, CF13TB (Wales)*

**Corresponding author: David E. Hibbs, david.hibbs@sydney.edu.au*

Abstract

Experimental charge density distribution studies of two polymorphic forms of piroxicam, β-piroxicam **(1)** and piroxicam monohydrate **(2)**, were carried out *via* high-resolution single crystal X-ray diffraction experiments and multipole refinement. The asymmetric unit of **(2)** consists of two discrete piroxicam molecules, **(2a)** and **(2b)**, and two water molecules. Geometry differs between **(1)** and **(2)** due to the zwitterionic nature of **(2)** which results in the rotation of pyridine ring around the C(10)–N(2) bond by approximately 180°. Consequently, the pyridine and amide are no longer co-planar and **(2)** forms two exclusive, strong hydrogen bonds, H(3) …O(4) and H(2) …O(3), with bond energy of 66.14 kJ mol^{-1} and 112.82 kJ mol^{-1} for **(2a)**, 58.35 kJ mol^{-1} and 159.51 kJ mol^{-1} for **(2b)** respectively. Proton transfer between O(3) and N(3) in **(2)** results in significant differences in surface electrostatic potentials. This is clarified on calculation of atomic charges in the zwitterion shows the formally positive charge of the pyridyl nitrogen is redistributed over the whole of the pyridine ring instead of concentrated at N-H. Similarly, the negative charge of the oxygen is distributed across the benzothiazinecarboxamide moiety. Multipole derived lattice energy for **(1)** is -304 kJ mol^{-1} and that for **(2)** is -571 kJ mol^{-1}, which is in agreement with the experimentally determined observations of higher solubility and dissolution rates of **(1)** compared to **(2)**.

Introduction

Polymorphism occurs when a compound exists in different crystal forms with the same chemical composition. In the past century, polymorphism of organic compounds, active pharmaceutical ingredients (API) in particular, has been extensively studied. At present, most pharmaceutical products are formulated in solid form, providing accurate dosage and easy storage but over half of these exhibit polymorphism.[1] The inconsistencies in physical properties displayed by pharmaceutical polymorphs, especially dissolution rate and solubility, are perceived as both a great source of frustration and intense interest for pharmaceutical scientists.

Piroxicam, (4-Hydroxy-2-methyl-N-(2-pyridinyl)-2H-1,2-benzothiazine-3-carboxamide 1,1-dioxide) is a potent non-steroidal anti-inflammatory drug (NSAID) that is widely used for pain relief in rheumatoid arthritis, osteoarthritis as well as other muscular pain and injuries. Its mechanism of action is preventing the production of prostaglandins by non-selectively inhibiting the enzymes cyclooxygenase (COX) 1 and 2, which are involved in inflammatory and pain responses in the body, and thus provides anti-inflammatory, analgesic and antipyretic activity.

Polymorphs of piroxicam were first reported back in 1982 by Mihalic *et al.* [2] They identified two anhydrous piroxicam polymorphs which exist in cubic and needle forms, as well as a monohydrate form that appears as yellow prisms. Since then, the polymorphism of piroxicam has been widely investigated leading to identification of a total of four anhydrous forms and one monohydrate form of piroxicam. While there have been significant efforts devoted to the discovery of the polymorphs of piroxicam, the characterisation and nomenclatures of piroxicam polymorphs have remained inconsistent and occasionally conflicting[3].

One of the reasons is that this may be due to the ready phase transition of the sample, leading to the miscorrelation between experimental characterisation and a specific polymorphic form. Another possible reason would be due to the close polytypic relationship between α_1 (orthorhombic, *Pca2₁, a=11.8, b=17.4, c=7.0*) and α_2 (monoclinic, *P2₁/c, a=17.6, b=11.9, c=7.0, β=97°*), where both were erroneously referred to as the single form II by Vrecer *et al.*[4] Sheth *et al.* attempted to resolve confusion between the polymorphic forms in a summary of reported properties of piroxicam polymorphs with detailed comparison of the hydrogen bonding profiles of form I and form II.[3] This was reinforced by Upadhyay and Bond with a detailed description of crystallisation conditions and other experimental characterisation data for piroxicam polymorphs α_1 and α_2.[5]

The US Food and Drug Administration (FDA) has produced some nonbinding recommendations in its Guidelines for Industry report[6], to assist in assessing what truly qualifies as a polymorph. In this guide, polymorphs include crystalline and amorphous forms, as well as solvates and hydrates. Bordner *et al.*[7] reported that unlike the previously reported structures, it exists in a zwitterionic form, with the enolic hydrogen on O(3) having been transferred to the pyridine nitrogen N(3) (Figure 1).

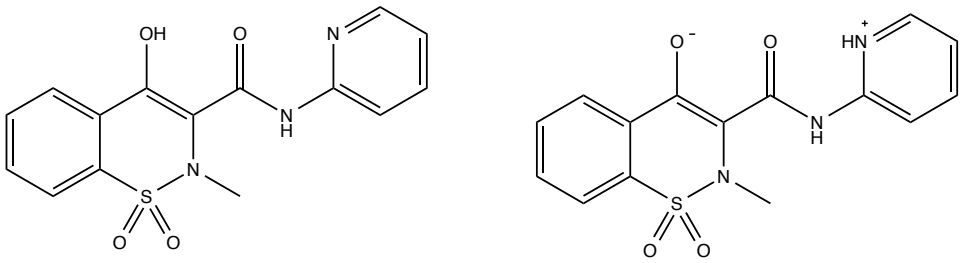

Figure 1. Structure of piroxicam (4-Hydroxy-2-methyl-N-(2-pyridinyl)-2H-1,2-benzothiazine-3-carboxamide 1,1-dioxide) (a) and its zwitterionic form (b).

The experimental electron density distribution (EDD) of a molecular system obtained from high-resolution X-ray diffraction experiments forms a unique physical-chemical method, which allows detailed information about the nature of intra- and intermolecular charge interaction in the solid state to be obtained. Bader's Atoms in Molecules (AIM)[8] approach provides an excellent tool for interpretation of both X-ray determined and theoretical charge densities. Analysis of the charge density is based upon the topological properties of the density ρ(r), where the topological analysis is based upon those bond critical points (BCP's) where the gradient of the density, $\nabla\rho$, vanishes. Properties evaluated at such points characterise the bonding interactions present, and have been widely used to study intermolecular interactions. The application of AIM allows not only the network of intermolecular contacts to be established, but also permits an estimation of their energy through the correlation between the energy and the electron density at the bond critical point.[9] It has been noted that there are a limited number of experimental charge density studies on polymorphic systems[10,11,12], due in the main to the difficulty in obtaining suitable crystals. In an attempt to provide more detailed characterisation of piroxicam polymorphs and to explain the difference in physical properties between the polymorphs, we report a comparison of the charge density distribution obtained from high-resolution single crystal X-ray diffraction on two polymorphs of piroxicam, form I, aka the β-form **(1)**, and the related monohydrate **(2)**. In this study, the experimental EDD between the two forms are compared with the aim of investigating if the changes in charges can be significant enough to be: (a) accurately determined, and (b) what are the structural implications of any charge redistribution.

Methods

Crystal preparation

Piroxicam was purchased from Sigma-Aldrich and used without further purification. Polymorphs **(1)** and **(2)** were obtained *via* slow evaporation from acetone, surprisingly, in the same vial.

X-ray Data Collection, Integration and Reduction

The single crystal X-ray diffraction experiments were carried out in the Faculty of Pharmacy at the University of Sydney using an Agilent SuperNova™ X-ray diffractometer with an X-ray wavelength of 0.7107 Å (Mo Kα) at 100K. Crystals of **(1)** and **(2)** with dimensions (0.30 x 0.20 x 0.20) mm and (0.25 x 0.15 x 0.15) mm respectively, were mounted onto the tip of a thin glass fibre with Paratone-N oil being used as both an adhesive and cryo-protectant. Data were collected for all crystals using 1° ω-scans maintaining the crystal-to-detector distance at 5.2cm for **(1)** and 5.3 cm for **(2)**. For **(1)** and **(2)**, reciprocal space coverage was achieved during the data collection by positioning the detector arm at two different angles in 2θ, 41.5° and 90.5°. Exposure times of 6 and 24 seconds were used for **(1)**, 15 and 30 seconds for **(2)** respectively. A total of 7695, and 4587, frames were collected for **(1)** and **(2)** respectively.

Integration and reduction of the collected data was performed with the CrysAlis^{Pro} software package.[13] All crystals were cooled to 100K with an Oxford Cryosystems COBRA cooler. The unit cell parameters for **(1)** were refined from 198191 reflections in the monoclinic space group $P2_1/c$ with Z=4, F(000) =688 and μ=0.248 mm^{-1}. The unit cell parameters for **(2)**, were refined from 456880 reflections in the triclinic space group $P\bar{1}$ with Z=2, F(000) =728 and μ=0.249 mm^{-1}. Refer to Table 1 for selected crystallographic information from the independent atom model (IAM) and multipole refinements. Bond lengths and angles,

temperature factors, coordinates, torsion angles and full hydrogen bond details can be found in supporting information tables S1-S12.

Table 1. Selected crystallographic information for complexes **(1)** and **(2)**.

	1	**2**
Formula	$C_{15}H_{13}N_3O_4S$	$C_{15}H_{13}N_3O_4S.H_2O$
Molecular Mass	331.34	349.34
Crystal size (mm)	0.25 x 0.20 x 0.20	0.25 x 0.15 x 0.15
Temperature (K)	100	100
Crystal system	Monoclinic	Triclinic
Space group	$P2_1/c$	P -1
a (Å)	7.034(1)	10.347(10)
b (Å)	14.989(1)	12.713(10)
c (Å)	13.894(1)	12.810(10)
α (^{o})	90	102.78(10)
β (^{o})	96.38(1)	99.99(10)
γ (^{o})	90	108.73(10)
Volume (Å^3)	1455.90(1)	1500.67(2)
Z	4	4
Refinement Method	Full-matrix least squares on F^2	Full-matrix least squares on F^2
No. of reflections collected	198191	456880
No. unique	16911	31885
R_{int}	0.045	0.021
Completeness (%)	95.8	99.6
No. reflections used	14742	23573
ρ_c (gcm^{-1})	1.512	1.546
F(000)	688	728
μ (mm^{-1})	0.248	0.249
sin θ/λ_{max}	1.11 Å^{-1}	1.11 Å^{-1}
θ range for data collection (°)	2.718 to 65.67	2.763 to 65.17
Index ranges	-17<=h<=18 -38<=k<=38 -34<=l<=35	0<=h<=22 -28<=k<=26 -28<=l<=35
IAM Refinement		
Final R1, wR2	0.034, 0.09	0.040, 0.105
Goodness of fit	1.045	1.061
Residual density (eÅ^{-3})	-0.739, 0.829	-0.717, 0.678

Multipole Refinement		
N_{obs}/N_{var}		
Exp	24.1	18.7
SH_D	24.3	28.6
$R(F)$, $R(F^2)$, all data		
Exp	0.021, 0.031	0.024, 0.026
SH_D	0.031, 0.032	0.024, 0.027
$R_w(F)$, $R_w(F^2) > 2\sigma(F)$		
Exp	0.023, 0.045	0.014, 0.029
SH_D	0.026, 0.050	0.015, 0.029
Goodness of fit		
Exp	1.707	1.558
SH_D	1.696	1.570
Residual density (eÅ^{-3})		
Exp	-0.25 to 0.27	-0.34 to 0.06
SH_D	-0.32 to 0.28	-0.25 to 0.25

Data refinement strategies

The structures of **(1)** and **(2)** were solved using direct methods (SHELXT).[14] For both, full matrix least squares refinement based on F^2 was performed using SHELXL-2015.[15] The bond lengths between non-hydrogen atoms to hydrogen atoms (X-H bonds, where X = C, O, N) were fixed at average values determined by neutron diffraction studies, taken from Allen *et al.,*[16] non-water O−H, N−H, and C−H bond lengths being 0.967, 1.009, and 1.083 Å respectively, with bond vectors taken from the original riding H-atom models in the IAM refinement. For the water molecules the O – H bond lengths were fixed at 0.985 Å.[17] All non-hydrogen atoms were refined anisotropically.

The coordinates and anisotropic temperature factors from the IAM were then imported into XD2006,[18] a program that utilises a least squares procedure to refine a rigid pseudoatom model in the form of the Hansen-Coppens multipole formalism.[19] In this formalism, the electron density, $\rho(\mathbf{r})$ within a crystal is described by the summation of aspherical

pseudoatoms (each with its own electron density) with nuclear positions r_j as shown in the Equation (1) below:

$$\rho(r) = \sum_j j\, \rho_j(r - R_j) \qquad (1)$$

The complete density of the pseudoatomic model is modelled by the following Equation (2):

$$\rho_j(r_j) = P_c\rho_c + \kappa'^3 P_v\rho_v(\kappa' r) + \kappa''^3 \sum_{l=0}^{l_{max}} \sum_{m=-l}^{m=1} P_{lm} R_l\,(\kappa'' r_j) d_{lmp}(\theta_j, \phi_j)$$

(2)

The expression for the pseudoatom density includes the usual spherical core, a term to describe the spherical component of the valence density, plus a deformation term describing the asphericity of the valence density. The radial functions { $R_l(r_j)$ } are modulated by angular functions { $d_{lmp}(\theta_j, \Phi_j)$ } defined by axes centred on each atom. A number of radial functions may be used, the most common being Slater-type functions given in Equation (3):

$$R_l(r) = N r^{n_l} exp(-\zeta_l\, r) \qquad (3)$$

The multipole refinement process began with an analysis of the results of higher order spherical atom refinement (usually sin θ/λ > 0.7A^{-1}), providing accurate atomic positions forming the basis for the remainder of the refinement.

Sulfur and other third row atoms are traditionally modelled by the standard n_l-set of (4,4,4,4,4), as these were originally modelled using single-ζ functions to model the valence density. We and others, have shown that this standard description can be problematic[20,21] with high residual electron density in the proximity of the sulfur atoms. The n_l-set for sulfur used here was (4,4,4,5,5)[22]. In addition, optimisation of the sulfur core electron density distribution was achieved by assigning a spherical expansion/contraction coefficient (κ′), to the 1*s*, 2*s* and

2*p* electrons, and allowed to refine. The value of ζ for sulfur was that of the free atom (7.278 $Å^{-1}$)[23].

As outlined above, it was necessary to optimise the standard description of sulfur in this refinement. Each sulfur atom (in individual piroxicam moieties) was split so that the core shells ($1s^2$, $2s^2$, $2p^6$) has a spherical expansion/contraction coefficient (κ′) and a fixed population, while the valence shell ($3s^2$, $3p^4$) had both spherical and aspherical κ values, as well as population refined. The suitability of this model is demonstrated in Table 2, where maximum and minimum residual errors are significantly smaller in most cases than those obtained from the standard model of sulfur.

Table 2 details the results of the refined κ values for the sulfur atoms in all three molecules, along with the associated monopole populations. For **(1)**, in a standard multipole model (MM) refinement, both the spherical and aspherical components of the valence density are expanded, when compared to that of the free atom. However, when a core-optimised approach is taken, the spherical component of the valence density is expanded, while the aspherical valence density is essentially the same when compared to that of the free atom.

Interestingly, in **(2)**, the situation is somewhat different, despite the similar chemical environment of the sulphonyl group. Here the valence density is expanded as is the aspherical component, when compared to the free atom.

Table 2. Expansion/contraction coefficients (κ) for sulfur. Values in parentheses refer to a standard un-optimised (n_l =4,4,4,4,4) refinement.

Atom Label	**κ´**	**κ´´**	**Population (*e*)**	**R(F)**	**Max/Min Residual** e Å^{-3}
Piroxicam (1)					
S(1)$_{valence}$	0.9498	1.0002	5.8561		
S(1´)$_{core}$	0.9846	1.0000	10.0000	0.0219	0.27/-0.25
	(0.9876)	(0.9746)	(5.7451)	(0.0217)	(0.34/-0.37)
Monohydrate (2a)					
S(1A)$_{valence}$	0.9479	0.9813	5.5608		
S(1B)$_{core}$	0. 9479	1.0000	10.0000	0.021	(0.34/-0.06)
	(0.9848)	(0.9132)	(5.6523)	(0.027)	(0.22/-0.35)
(2b)					
S(1'A)$_{valence}$	0. 9479	0.9813	5.5142		
S(1'B)$_{core}$	0. 9479	1.0000	10.0000		
	-	-	(5.7177)		

The refinement proceeded by increasing the level of the multipole expansion in a stepwise manner, finally being truncated at the octapole level (l_{max} = 3) for C, O, N and S. Each C, O, N and S atom was assigned a kappa prime (κ′, a spherical function which governs expansion/contraction of the valence shell) during the refinement to allow for accurate modeling of the electron density, and finally a κ″ which models the aspherical radial expansion/contraction of the valence electrons. The density of hydrogen atoms was modeled using a single monopole, with κ′ fixed at 1.2, with the aspherical density modeled by a single

bond-directed dipole (l_{max} = 1). The refinements were continued until convergence was reached for each multipole before the next one was introduced. The Hirshfeld rigid bond test was used to determine if the anisotropic displacement parameters were of any actual physical xsignificance; *i.e.* has the electron density been successfully deconvoluted from the inherent thermal smearing.[24] This test measures the differences in mean-squared displacement amplitudes (DMSDA) with ADP's deemed to be described as physically meaningful if they are below 1 x 10^{-3} Å^2. The average value obtained from these refinements is 2.6 x 10^{-4} Å^2. Scale and temperature factors were refined separately from the multipoles, and only in the final cycles were all parameters allowed to refine together, to get the complete variance-covariance matrix, thus obtaining meaningful su's. Only reflections with intensity of F > 3σ (F) were included in the refinement. This model is termed *Exp* in the remainder of the manuscript. See Figure 2 for molecular structures of β-piroxicam and piroxicam monohydrate.

Anisotropic Temperature Factor Refinement of Hydrogen Atoms

The temperature factors of hydrogen atoms were also anisotropically modelled based upon discussions by Hoser *et al.,*[25] Spackman *et al.*[26] and Koritsansky *et al.*[27] These studies have observed dissimilarities in the topological analysis of weak interactions such as H-bonds, van der Waals forces and π- π stacking interactions.[28] To observe the effect of applying calculated anisotropic temperature factors for hydrogen atoms during multipole refinement, anisotropic temperature factors were calculated[29] and the resulting anisotropic displacement parameters (ADPs) transferred to the multipole model. This will be termed SH_D for the remainder of the manuscript. The anisotropic temperature factors for the hydrogen atoms were calculated using the SHADE3 server.[29] The multipole analyses with the anisotropic temperature factors

for hydrogen were truncated at the same level as above ((l_{max} = 3) for heavy atoms and up to the (l_{max} = 1) for hydrogen atoms). The multipole refinement for hydrogen atoms was capped at the dipolar level of expansion, as in this particular case, when expanded to the quadrupolar level, the populations were negligible. Refer to Table S13 in supplementary data for the ADPs used. As can be seen from Table 1, there is very little to separate the *Exp* and SH_D refinements, in a similar fashion to recent experiences[30,31] with calculated hydrogen ADPs in multipole refinements, the SH_D refinement was not able to locate critical points of some intramolecular hydrogen bonds and so the topological analysis will be based on the *Exp* refinement.

Computational Methods

Gas phase single point (SP) calculations were carried out on **(1)** and **(2)**, with the geometry taken from the high-order experimental coordinates. Calculations were performed with the Gaussian 09 suite[32] at the 6-311++G(d,p) level of theory for all structures. All calculations utilised the CAM-B3LYP[33,34,35]_which combines the hybrid B3LYP with the long range correction of Tawada *et al*.. Analysis of the topology of electron density from the experimental model was performed using the XDPROP module of XD2006,[18] while analysis of the electron density for the theoretical densities was performed using the AIMALL[36] package.

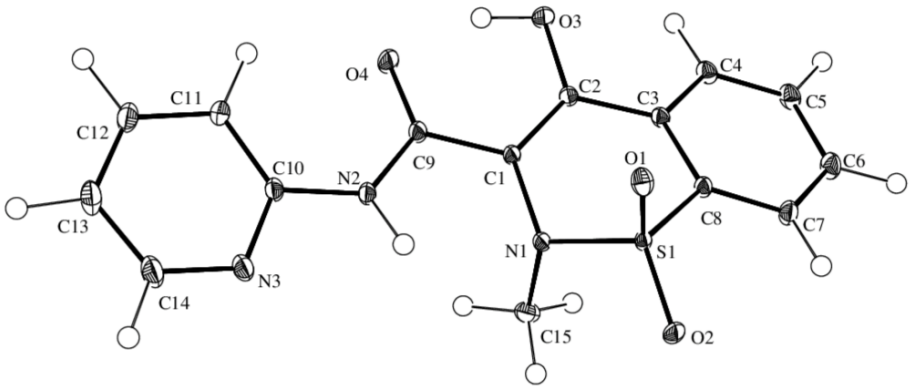

(1)

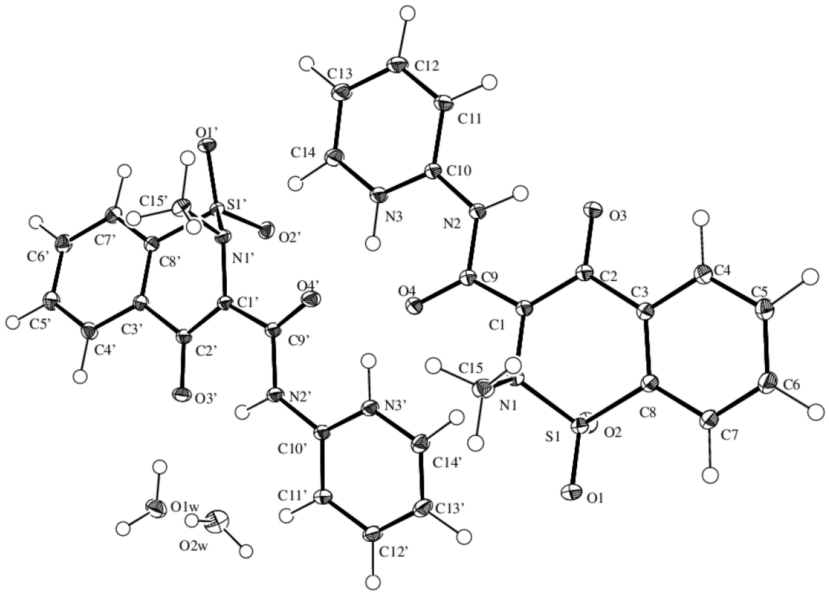

(2)

Figure 2. ORTEP diagram of β-piroxicam **(1)** and piroxicam monohydrate **(2)**. Thermal ellipsoids are shown at 50% probability level.[37]

Results and Discussion

Geometry

Bond lengths and angles for all experimental structures were obtained from the MM refinement output, for **(1)**, the X-ray structure was in excellent agreement with results reported by Koji-Prodic *et al.*[38] in 1982, with mean differences of 0.06Å and 0.4° for bond lengths and angles, respectively. A similar situation was also seen for **(2)**, where the geometrical details obtained from MM refinement were in good agreement with the bond lengths and angles reported by Bordner *et al.*[7] with mean differences of 0.12Å for bond length and 0.11° for angles, respectively. In the crystal of **(2)**, there are two independent molecules of piroxicam, both of which are zwitterionic in nature, where the enolic hydrogen (H3A) from O(3) is now found on the pyridyl nitrogen N(3). This has the effect of rotating the pyridyl group approximately 180° around the N(2) – C(10) bond (compared to **(1)**), and forms an intra-molecular hydrogen bond with the amide oxygen O(4). The effect of the intramolecular hydrogen bond can be seen in the bond lengths of 1.41Å and 1.37Å in (1) and (2) respectively for the N(2) – C(10) bond, with the bond in (2) being shorter due to increased attraction force between the surrounding atoms pulling the molecule closer together. Refer to Table S2 for **(1)** and S8 for **(2a)** and **(2b)** in supplementary data for a comparison of experimental bond lengths and angles.

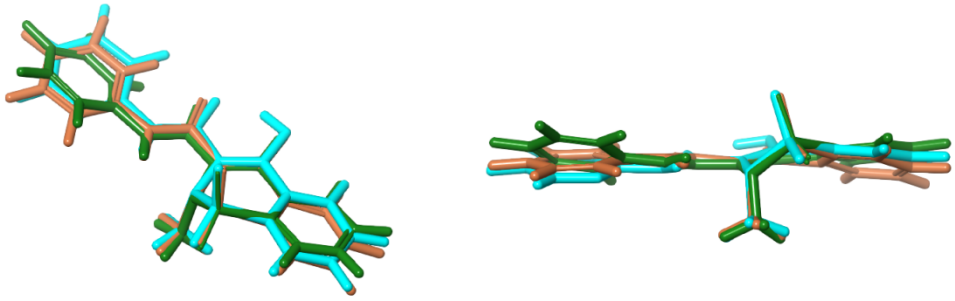

Figure 3. Structure overlays of **(1)** blue, **(2a)** green, and **(2b)** brown.

In **(1)**, the amide and pyridine fragments are essentially co-planar, as determined by theC(9)-N(2)-C(10)-C(11) torsion angle of -4.01°. In contrast, as noted by Bordner, the zwitterionic **(2a)** in **(2)** is markedly non-planar (C(1)-C(9)-N(2)-C(10) = 170.1°, see Figure 3, while **(2b)** retains an essentially planar conformation. Our high-resolution data allows us to examine the effects of this non-planarity on conjugation across the piroxicam molecule in its different polymorphs, along with those associated with the change in protonation state and crystalline environment. Properties at selected bond critical points within both forms are reported in Table 3 in order to probe these effects. Significant differences in bonding between forms are apparent in many bonds: **(1)** exhibits marked asymmetry in S—O bonds, apparently due to intermolecular hydrogen bonding (vide infra), which is not present in **(2)**. In addition, the formally double C(2)—C(3) bond is weaker in **(2)**, while C(2)—O(3) is stronger, suggesting that charge is substantially redistributed about this group and that formal assignment as an enolate in **(2)** may be problematic. A possible explanation of the stronger C(2) – O(3) bond in **(2)** is the resonance that occurs from the loss of the hydrogen atom to the nitrogen, resulting in increased electron density and subsequently increased bond strength. This explanation is further strengthened via a study of the bond orders of the C(2) – O(3) bonds and its surrounding bonds C(1) – C(2) and C(2) – C(3). According to Bader[8], a formal single bond should have ε=0.0 and a double bond ε=0.4. The C(1) – C(2) and C(2) – C(3) bonds in both **(2a)** and **(2b)** have minimally reduced double bond character compared to its counterpart in **(1)**, (ε=0.38 and 0.39) respectively for the aforementioned bonds in **(2a)** and **(2b)** *vs*. ε=0.42 in **(1)**). Following on from this, the ellipticity of the C(2) – O(3) bond was found to have marginally increased double bond character (ε=0.17 and 0.18 in **(2a)** and **(2b)** *vs.* ε=0.15 in

(1)) In the situation of the zwitterionic nitrogen. N(3), the addition of the hydrogen seems to have had little effect on the bond order or ellipticity (ε= 0.17,0.19 and 0.16 for C(10) – N(3) in **(1)**, **(2a)** and **(2b)** respectively and ε=0.16. 0.14 and 0.13 for C(14) – N(3) in **(1)**, **(2a)** and **(2b)**). A similar situation was seen in the theoretical models of **(1)** and **(2)**, which utilised delocalisation indices to determine bond order as discussed by Firme *et al.*[39]. Conjugation effects appear to be relatively small: C(1) – C(9) and C(9) – N(2) are very similar between forms, although N(2) – C(10) is slightly stronger in **(2)** than in **(1)**. Other than the case of C(2) – C(3) noted above, C – C bonds differ little between forms.

Figures 4(a-d) show the static deformation density maps (defined as: $F_{calc,\ multipole} - F_{calc,\ IAM}$) for **(1)** and **(2a)**, (**(2b)** being almost identical). The quality of refinement is reflected in the fact that there are no double maxima present in any bonding regions .In Figure 4(a), the O(3)–H(3A) can be clearly seen, while there is an intense maxima located on S(1). In Figure 4(b), the lone pair region of the pyridyl nitrogen is clearly visible. Of interest also in Figure 4(b), the polarisation of the lone pair on O(4) can be clearly seen participating in the hydrogen bond with H(11). Figure 4(c) is notable as the out-of-plane lone pair of O(3) can be seen directed at the amide H(2), however this can been seen more clearly in Figure 4(d), where the O(3) lone pairs show clear polarisation toward, this amide hydrogen, and additionally, to the H(1W) of the water molecule.

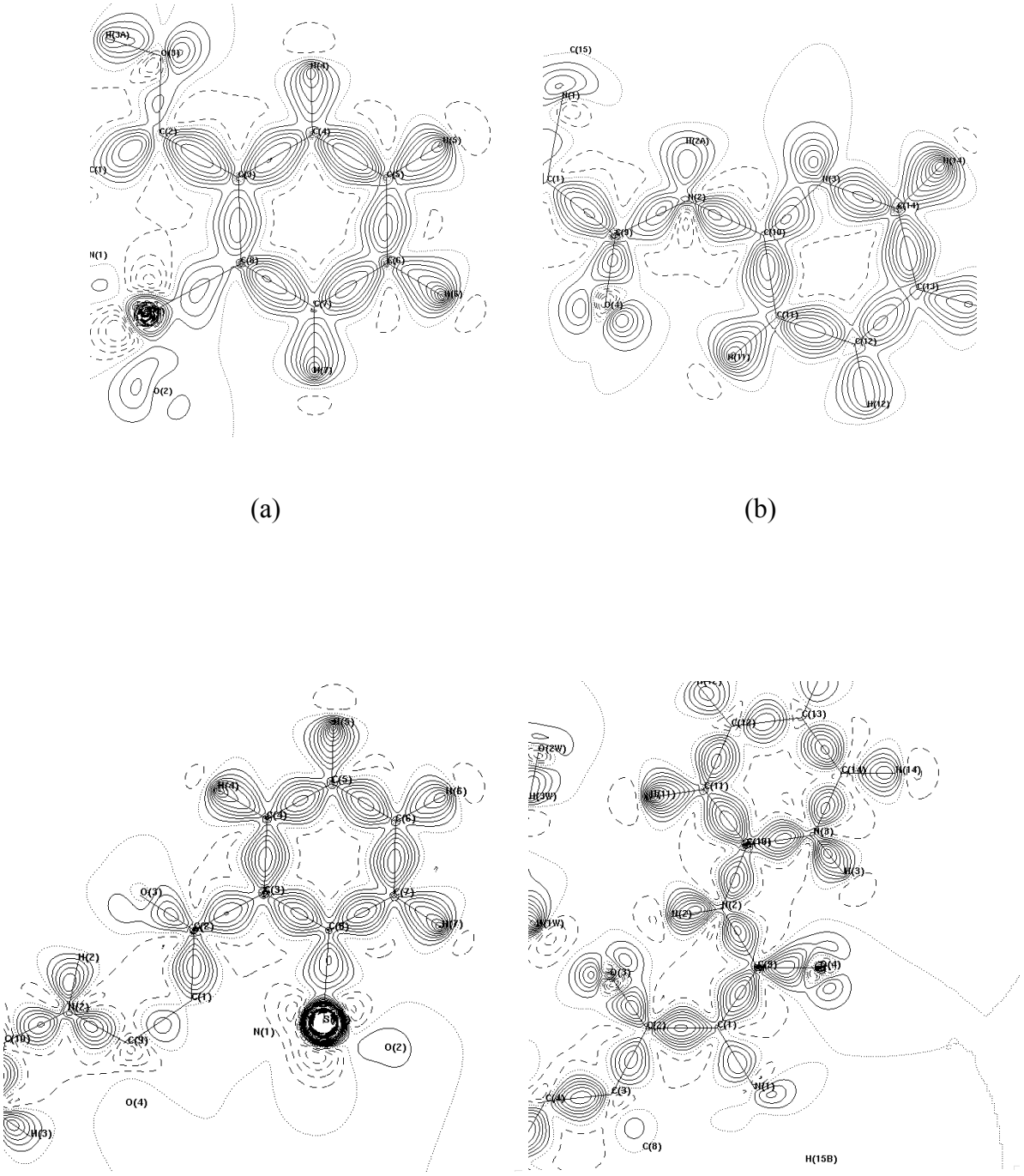

Figure 4. Deformation density of **(1)** (a), (b) and **(2a)** (c), (d)

Topological Analysis

Topological analysis of both the theoretical and experimental structures density was carried out and completeness of the analysis was ensured through satisfaction of the Poincaré-Hopf or its crystalline equivalent Morse relationship.[40] Table 3 details the topological data for **(1)** and **(2)**. While **(1)** is a neutral molecule and **(2a)** and **(2b)** are zwitterionic, perhaps unsurprisingly there is little difference in the values of ρ and $\nabla^2\rho$ in the bulk of the molecule (average difference of 0.10 eÅ^{-3} and 3.00 eÅ^{-5} for for ρ and $\nabla^2\rho$ respectively). Topological analysis of the experimental model shows the transfer of this proton results in a difference in ρ and $\nabla^2\rho$ around the O(3) – C(2) bond between **(1)** and **(2a)** as well as **(1)** and **(2b)**. **(2a)** and **(2b)** has a ρ greater than **(1)** by 0.487 eÅ^{-3} and 0.512 eÅ^{-3} respectively, and a $\nabla^2\rho$ greater than by 12.747 eÅ^{-5} and 10.451 eÅ^{-5} respectively. This suggests that the electron density is more localised and concentrated around the O(3) – C(2) bond as the electron density is no longer shared with enolic hydrogen due to the zwitterionic nature of **(2)**. In the same manner, ρ and $\nabla^2\rho$ around the N(3) – C(10) bond is significantly different due to the protonation of the atom. The value of ρ around N(3) – C(10) of **(2a)** and **(2b)** is 0.086 eÅ^{-3} and 0.017 eÅ^{-3} smaller than that of **(1)** respectively, while $\nabla^2\rho$ around the same bond of **(2a)** and **(2b)** is 10.865 eÅ^{-5} and 8.644 eÅ^{-5} smaller than that of **(1)** respectively. This once again suggests the electron density is now shared among N(3) – H(3A) as well as N(3) – C(10). See Table S14a in supplementary data for full details of *Exp*, SH_D and theoretical values for the topological analysis.

Table 3. Bond critical point data for selected bonds (all heavy atoms + O-H & N-H)

Bond	ρ	$\nabla^2\rho$	ε

	/ eÅ^{-3}	/ eÅ^{-5}	
S(1)-O(1) **(1)**	2.390	1.468	0.17
(2a)	2.246	10.506	0.05
(2b)	2.193	8.627	0.05
S(1)-O(2)	1.966	15.86	0.21
	2.168	11.575	0.08
	2.289	11.958	0.07
S(1)-N(1)	1.584	-10.92	0.35
	1.591	-5.826	0.14
	1.539	-3.963	0.19
S(1)-C(8)	1.392	-7.25	0.15
	1.453	-9.392	0.14
	1.402	-8.625	0;.13
O(3)-C(2)	2.060	-18.003	0.15
	2.547	-30.748	0.17
	2.572	-28.451	0.18
O(3)-H(3A)	2.255	-24.804	0.01
	-	-	-
	-	-	-
O(4)-C(9)	2.618	-28.284	0.09
	2.750	-27.384	0.16
	2.702	-32.154	0.14
N(1)-C(1)	1.760	-9.325	0.09
	1.845	-13.831	0.16
	1.813	12.996	0.14
N(1)-C(15)	1.622	-8.585	0.12

	1.716	-10.497	0.07
	1.757	-11.204	0.14
N(2)-C(9)	2.127	-21.430	0.17
	2.108	-24.344	0.19
	2.063	-23.611	0.17
N(2)-C(10)	2.083	-19.742	0.17
	2.185	-24.406	0.21
	2.181	-24.189	0.19
N(2)-H(2A)	2.355	-23.319	0.07
	2.194	-33.314	0.06
	2.188	-28.823	0.07
N(3)-C(10)	2.264	-17.885	0.17
	2.346	-28.746	0.19
	2.277	-26.524	0.16
N(3)-C(14)	2.389	-22.930	0.16
	2.194	-26.468	0.14
	2.161	-25.410	0.13
N(3)-H(3)			
	1.989	-30.811	0.05
	2.137	-35.185	0.06
C(1)-C(2)	2.238	-21.422	0.42
	2.177	-21.804	0.38
	2.057	-18.055	0.39
C(1)-C(9)	1.909	-14.883	0.29
	1.966	-17.923	0.35
	1.997	-18.336	0.33

C(2)-C(3)	1.957	-16.253	0.24
	1.730	-13.551	0.21
	1.724	-13.151	0.17
C(3)-C(4)	2.052	-18.061	0.27
	2.122	-20.211	0.25
	2.092	-19.540	0.23
C(3)-C(8)	1.900	-15.073	0.18
	2.076	-19.407	0.25
	2.059	-18.786	0.29
C(4)-C(5)	2.164	-20.379	0.28
	2.100	-19.848	0.23
	2.085	-20.048	0.28
C(5)-C(6)	1.996	-18.044	0.19
	2.100	-19.468	0.26
	2.118	-19.775	0.26
C(6)-C(7)	2.094	-18.640	0.21
	2.136	-20.090	0.22
	2.143	-20.440	0.24
C(7)-C(8)	2.140	-18.671	0.24
	2.104	-20.004	0.27
	2.059	-18.786	0.29
C(10)-C(11)	2.081	-18.549	0.28
	2.113	-20.542	0.26
	2.095	-19.392	0.26
C(11)-C(12)	2.190	-20.303	0.21
	2.174	-21.572	0.23

	2.140	-20.589	0.26
C(12)-C(13)	2.007	-16.428	0.19
	2.100	-19.713	0.17
	2.047	-18.686	0.19
C(13)-C(14)	2.147	-19.746	0.23
	2.253	-24.130	0.26
	2.236	-23.069	0.27

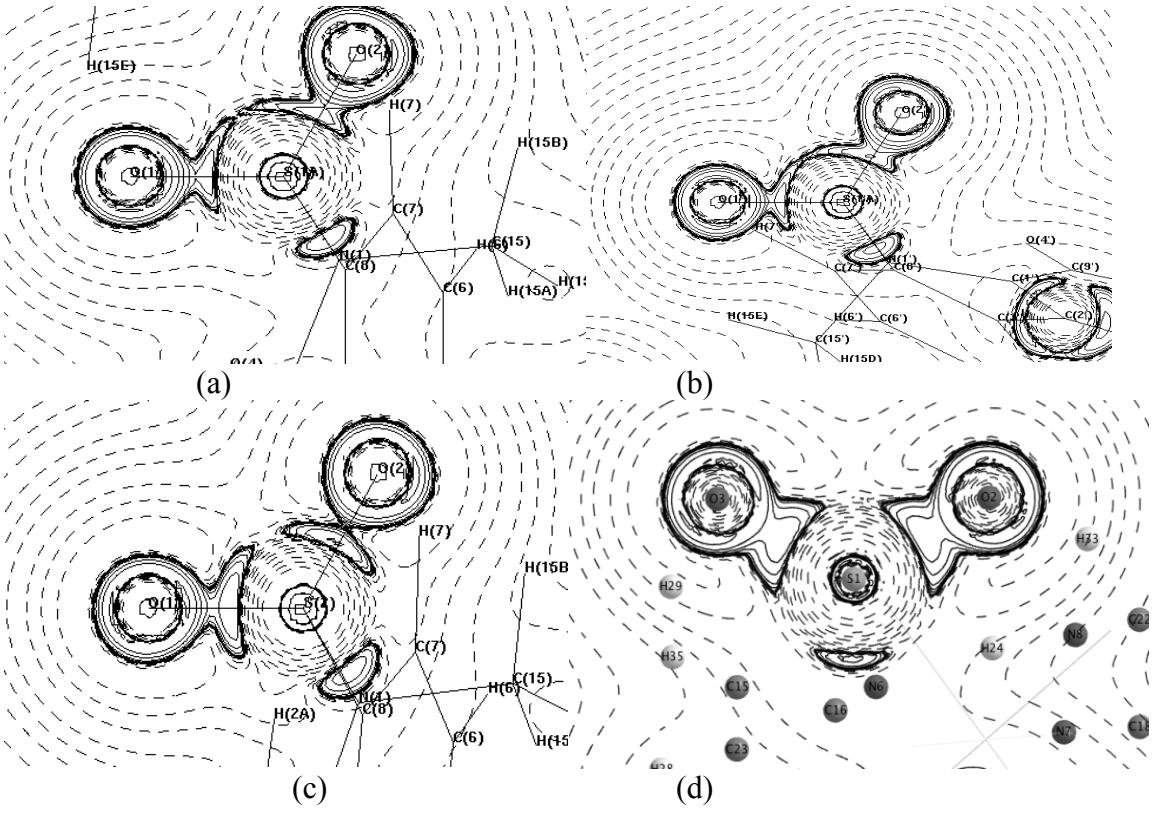

Figure 5. *Exp* $-\nabla^2\rho_{bcp}$ distribution of the O(1) – S(1) – O(2) plane for piroxicam in (a) **(1)**, (b) **(2a)**, (c) **(2b)**, (d) theoretical for **(1)**.

Overall, the agreement in the topological analysis between experiment and theory is good. The difference in ρ_{bcp} and $\nabla^2\rho_{bcp}$ values obtained from the *Exp* and theoretical single point densities for both **(1)** and **(2)**, in non- S-O bonds (excluding bonds to hydrogen atoms), show

average differences of -0.05 eÅ^{-3} and -0.02eÅ^{-5} and 4.08 eÅ^{-5} and -1.54 eÅ^{-5} ρ_{bcp} and $\nabla^2\rho_{bcp}$, respectively.

In the S–O bonds however, agreement between experiment and theory is poor. For **(1)** the largest differences seen are in the topology of the sulfonyl bonds, Density Functional Theory (DFT) underestimates ρ_{bcp} by 0.34 eÅ^{-3} in S(1) – O(1), and overestimates this quantity in S(1) – O(2) by 0.1 eÅ^{-3}. Even larger differences in $\nabla^2\rho_{bcp}$ are found, where the experimental values are underestimated by 27 and 13 e Å^{-5} for the same bonds. For **(2)**, the effect on the sulfonyl bonds Laplacian values are similar, and differences in $\nabla^2\rho_{bcp}$ values between experiment and DFT for the S=O bonds in **(2a)** were 21 and 19 eÅ^{-5}, while for **(2b)** the values were 23 and 20 eÅ^{-5}. However, interpretation of such values obscured by the rapidly changing nature of $\nabla^2\rho$ within polar covalent bonds, where the BCP is often located close to the point where $\nabla^2\rho$ changes sign.

Experimental and theoretical $-\nabla^2\rho$ distributions of the O(1)–S(1)–O(2) plane are shown in Figures 5(a-d), with the clear disagreement between experimental and theoretical models is both seen in **(1)** and **(2)**. DFT universally predicts large, positive values of $\nabla^2\rho_{bcp}$, (d), indicative of closed-shell interactions, and the experimental maps show a similar pattern. As shown in Figure 5, Laplacian diagrams for S=O bonds in each of the complexes show a clear overlap of the valence shell charge concentration, resulting in what appears to be open shell interactions, albeit with a severe pinching off in the S(1)–O(2) bond in **(2a)**. This is not uncommon in polar bonds, as we have previously noted[41] and can be explained by the experimental density changing more quickly than the theoretical counterpart. Thus, very small differences in the total electron density, of the same magnitude as the residual errors stemming from the multipole model, are amplified in the Laplacian into apparently major discrepancies between experiment and theory[20, 41].

Topology of hydrogen bonds

As well as the non-planarity of **(2)** compared to **(1)**, the transfer of a proton from O(3) to N(3) induces a 180° rotation of the pyridine group and establishes a quite different pattern of intra- and intermolecular hydrogen bonding between polymorphs. Details of these hydrogen bonds, as determined by properties of the associated bond critical points, are reported in Tables 4 and 5, for **(1)** and **(2)** respectively. Form **(1)** contains three intramolecular H-bonds of type O—H…O, N—H…N and C—H…O. According to the data in Table 4, the former is exceptionally strong with very large electron density and positive Laplacian, along with negative energy density. Application of Abramov and Espinosa's method for estimation of H-bond strengths[9,42] results in a very large stabilisation energy of almost 160 kJ mol^{-1} (38 kcal mol^{-1}) for this interaction, placing it at the upper limit of values considered typical for H-bonds[43]. The other two intramolecular H-bonds are weaker but still stabilise the planar form of **(1)** by *ca.* 30 and 50 kJ mol^{-1}, respectively. The method has previously been criticised for intramolecular H-bonds[31], so complementary DFT calculations were performed. Rotation of 90° about the C(1)—C(9) bond breaks both the O—H…O and N—H…N H-bonds, but keeps the C—H…O contact. This (hypothetical) rotated form of piroxicam is found to be 81 kJ mol^{-1} less stable than the true form. This value should contain contributions from disrupted conjugation as well as broken H-bonds, and so is likely to be an overestimation of the strength of the latter. It is therefore striking that the DFT prediction is approximately half of that from electron density, such that we once again call into question the use of Abramov's method for strong intramolecular H-bonds. Spackman recently broached this subject via an analysis of intermolecular interaction energies calculated via the Abramov-Espinosa method and the PIXEL method initially introduced by Gavezzoti[44]. Spackman found that the Abramov-Espinosa method often overestimated the strength of interactions[45], especially those involving heavy atoms such as halogens, whereas the PIXEL methods' use of interatomic

separation to estimate interaction energies correlated significantly better with theoretical energies.

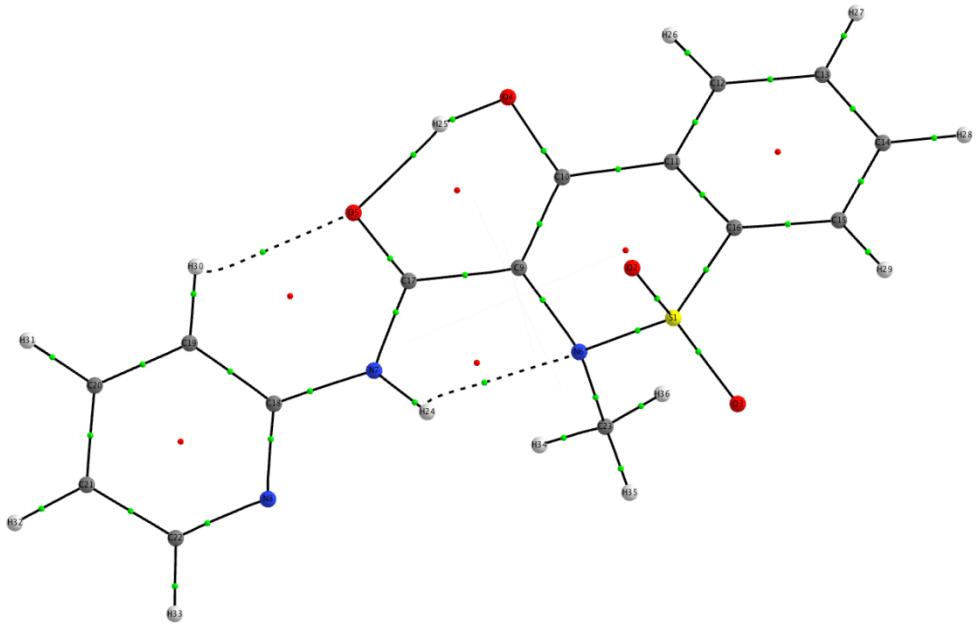

Figure 6. Intramolecular interactions in β-piroxicam **(1)**[36].

Table 4. Topological analysis of hydrogen bonding in **(1)**. Standard uncertainties have been omitted from the table for clarity. They are closely scattered around 0.02 eÅ^{-3} (ρ_{bcp}) and 0.05 eÅ^{-5} ($\nabla^2\rho_{bcp}$).

	ρ / eÅ^{-3}	$\nabla^2\rho$ / eÅ^{-5}	ε	G / E_h eÅ^{-3}	V / E_h eÅ^{-3}	H / E_h eÅ^{-3}	E_{HB} / kJ mol^{-1}
Intramolecular							
N(2) - H(2A) ⋯ N(1)	0.16	2.18	1.91	0.14	-0.13	0.01	50.57
O(3) - H(3A) ⋯ O(4)	0.36	5.03	0.03	0.38	-0.41	-0.03	159.51
C(11) - H(11) ⋯ O(4)	0.12	1.60	0.14	0.10	-0.08	0.02	31.12
Intermolecular							
N(2)–H(2A) ⋯ O(2)$^{\#1}$	0.07	1.24	0.33	0.07	-0.05	0.02	19.45
C(5) – H(5) ⋯ O(2)$^{\#2}$	0.05	0.75	0.43	0.04	-0.03	0.01	11.67
C(5) – H(5) ⋯ O(1)$^{\#3}$	0.04	0.73	0.53	0.04	-0.03	0.01	11.67

C(14) – H(14) ⋯ O(4) [#4]	0.01	0.43	2.27	0.02	-0.01	0.01	3.89
C(15) – H(15A) ⋯ O(1) [#5]	0.04	0.67	0.09	0.03	-0.02	0.01	7.78
C(15) – H(15B) ⋯ O(1) [#6]	0.05	0.74	0.11	0.04	-0.03	0.01	11.67
Close Contacts							
C(3) ⋯ C(12) [#7] π ⋯ π	0.03	0.31	0.46	0.02	-0.01	0.00	3.89
C(4) ⋯ C(10) [#8] π ⋯ π	0.04	0.35	3.56	0.02	-0.01	0.01	3.89
C(5) ⋯ C(9) [#9] C=O ⋯ π	0.04	0.34	0.48	0.02	-0.01	0.00	3.89
H(12) ⋯ H(6) [#10]	0.01	0.59	0.13	0.03	-0.02	0.01	7.78
H(11) ⋯ H(15C) [#7]	0.02	0.32	0.47	0.02	-0.01	0.01	3.89

[#]Symmetry operators used to define atoms: [1]-x,1-y,-z; [2]-x,1/2+y,1/2-z; [3]x,1/2-y,-1/2+z; [4]-1-x,-1/2+y,-1/2-z; [5]-1+x,y,z; [6]-x,1-y,-z; [7]-1+x,1/2-y,-1/2+z; [8]x,1/2-y,1/2-z; [9]x,1/2-y,-1/2+z; [10]-1+x,y,-1+z.

Proton transfer alters the pattern of intramolecular H-bonds markedly, with **(2)** exhibiting two intramolecular N—H…O interactions within each of the two independent piroxicam molecules. These bonds are predicted to be very strongly stabilising on the basis of density properties at the corresponding bond critical points. Application of Abramov and Espinosa's method predicts H-bond strengths of 66 and 112 kJ mol^{-1} for N(3)—H(3)…O(4) and N(2)—H(2)…O(3), respectively, again placing them at the upper end of typical stabilisation energies. Interestingly, these values in **(2b)** are 58 and 159 kJ mol^{-1} for N(3')—H(3')…O(4') and N(2')—H(2')…O(3'), respectively. While the difference of -8 kJ mol^{-1} for the first of these could be down to the very subtle geometric differences, the -47 kJ mol^{-1} difference in the latter bonds may possibly be attributed to O(3) participating in two additional strong hydrogen bonds; the intermolecular interaction within the asymmetric unit O(1W)–H(1W)…O(3) (51 kJ mol^{-1}), and C(15)–H(15A)…O(3) (113 kJ mol^{-1}) between molecules in adjacent unit cells. Overall, these assignments are supported by DFT, from which we predict destabilisation due to rotation about relevant bonds (C(10)—N(2) and C(1)—C(9)) of 104

and 166 kJ mol^{-1}, in better agreement with the Abramov predictions. It is interesting to note that both prediction methods suggest stronger interaction between the (formally) neutral N(2)—H(2) and negative O(3), than between the cationic N(3)—H(3) and neutral O(4), in line with the shorter H…O distance in the former. It must be noted here that **(2)** has a far greater number of interactions in total, and this will be discussed in the next section.

The distribution of charge in the two forms of piroxicam, and any relation to the formal charges expected of neutral and zwitterionic forms, which ultimately gives rise to this difference is discussed in more detail below.

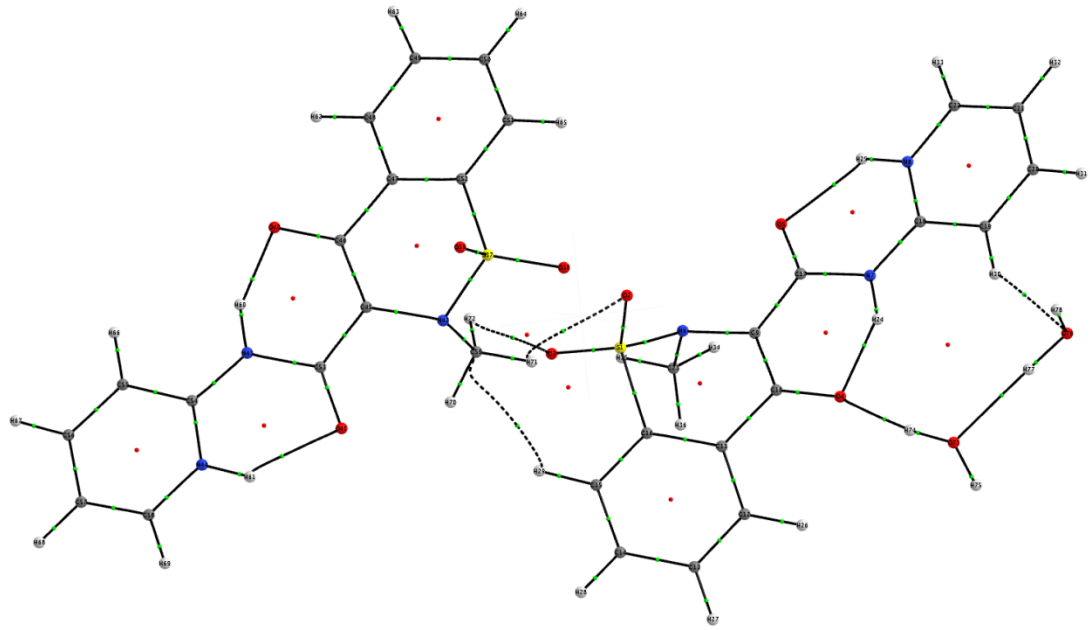

Figure 7. Intra- and intermolecular interactions in piroxicam monohydrate **(2)**[36].

Table 5. Topological analysis of hydrogen bonding in **(2)**. Standard uncertainties have been omitted from the table for clarity. They are closely scattered around 0.02 e $Å^{-3}$ (ρ_{bcp}) and 0.05 e $Å^{-5}$ ($\nabla^2\rho_{bcp}$).

	ρ / e$Å^{-3}$	$\nabla^2\rho$ / e$Å^{-5}$	ε	G / E_h e$Å^{-3}$	V / E_h e$Å^{-3}$	H / E_h e$Å^{-3}$	E_{HB} / kJ mol^{-1}
Intramolecular							
N(3) - H(3) ⋯ O(4)	0.20	2.71	0.04	0.18	-0.17	0.01	66.14
N(2) - H(2) ⋯ O(3)	0.27	4.66	0.15	0.31	-0.29	0.02	112.82
N(3') - H(3') ⋯ O(4')	0.17	2.39	0.12	0.16	-0.15	0.01	58.35
N(2') - H(2') ⋯ O(3')	0.35	5.62	0.06	0.40	-0.41	-0.01	159.51
Asymmetric unit intermolecular							
C(15') - H(15E) ⋯ O(1)	0.05	0.53	0.24	0.03	-0.02	0.01	7.78
C(15') - H(15F) ⋯ O(2)	0.02	0.33	0.56	0.01	-0.01	0.00	3.89
C(7) - H(7) ⋯ C(15')	0.03	0.34	0.96	0.02	-0.01	0.00	3.89
O(1W) - H(1W) ⋯ O(3)	0.09	4.52	0.58	0.22	-0.13	0.09	50.57
O(2W) - H(3W) ⋯ O(1W)	0.11	2.92	0.05	0.16	-0.11	0.05	42.79
C(11) - H(11) ⋯ O(2W)	0.05	0.82	0.69	0.04	-0.03	0.01	11.67
Intermolecular							
C(15)-H(15A)...O(3)	0.28	4.38	0.05	0.3	-0.29	0.00	112.83
O(1W)-H(1W)...O(4)	0.11	3.25	0.13	0.17	-0.12	0.05	46.69
O(2W)-H4(W)...O(1W) [#1]	0.11	3.252	0.13	0.17	-0.12	0.05	46.69
N(3)-H(3)..O(4') [#2]	0.11	1.648	0.05	0.1	-0.08	0.02	31.12
N(3)-H(3)…O(2') [#3]	0.07	1.023	0.39	0.06	-0.05	0.01	19.45

C(14)-H(14)…N(1') [#2]	0.03	0.569	1.36	0.03	-0.02	0.01	7.78
C(14')-H(14')…O(4) [#2]	0.05	0.722	0.27	0.04	-0.03	0.01	11.67
C(14')-H(14')…N(1) [#2]	0.01	1.205	0.00	0.06	-0.03	0.03	11.67
Close contacts							
C(11)…C(4') [#3]	0.03	0.32	0.29	0.02	-0.01	0.00	3.89
	0.03	0.31	1.96	0.02	-0.01	0.00	3.89
C(4')…C(10') [#4]	0.03	0.34	2.47	0.02	-0.02	0.00	7.78
	0.04	0.34	0.89	0.02	-0.02	0.00	7.78
C(12')…O(1') [#5]	0.05	0.72	0.86	0.04	-0.03	0.01	11.67
	0.05	0.714	0.07	0.04	-0.03	0.01	11.67
C(12)…O(3') [#3]	0.06	0.790	0.11	0.05	-0.04	0.01	15.56
	0.06	0.772	1.02	0.04	-0.03	0.01	11.67
C(13)…O(3') [#3]	0.06	0.79	1.16	0.05	-0.04	0.01	15.56
	0.06	0.772	1.02	0.04	-0.03	0.01	11.67
C(7')…O(1) [#3]	0.05	0.752	1.16	0.04	-0.03	0.01	11.67
	0.03	0.448	0.26	0.02	-0.02	0.01	7.78
C(14')…O(4) [#2]	0.06	0.910	0.23	0.05	-0.04	0.01	15.56
	0.04	0.549	0.16	0.03	-0.02	0.01	7.78
C(15)…H(14') [#2]	0.04	0.667	0.00	0.05	-0.02	0.01	7.78
	0.01	1.571	0.00	0.07	-0.04	0.04	15.56
C(7)…H(15B) [#6]	0.05	0.508	3.86	0.03	-0.02	0.01	7.78
	0.05	0.521	0.86	0.03	-0.02	0.01	7.78

[#]Symmetry operators used to define atoms: [1]1-x,3-y,1-z; [2]1+x,1+y,z; [3]1-x,2-y,-z; [4]1-x,1-y,-z; [5]x,-1+y,z; [6] 2-x,2-y,1-z.

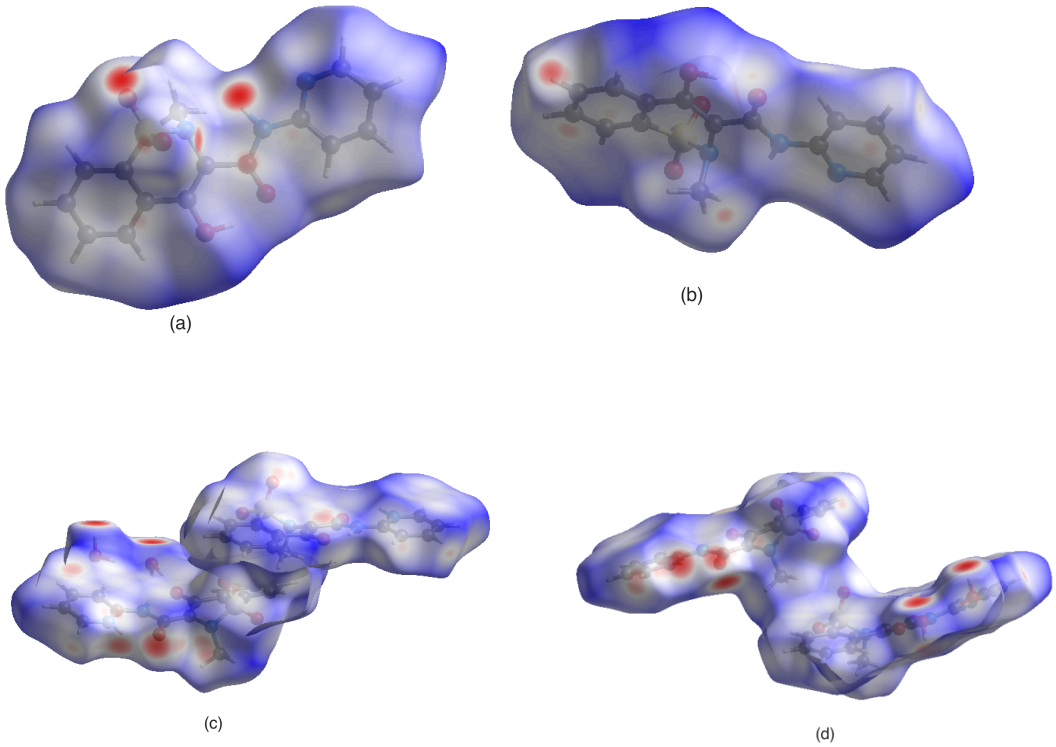

Figure 8. Hirshfeld surfaces for **(1)** (a), (b) and **(2)** (c), (d).

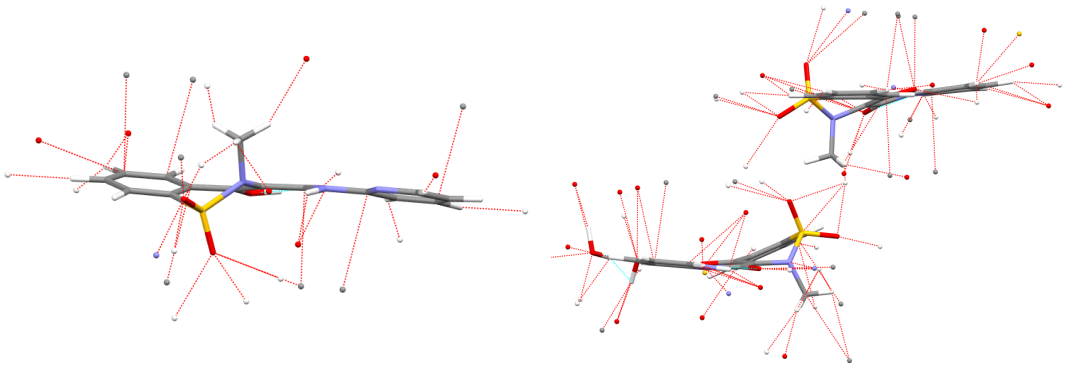

(a) (b)

Figure 9. Hydrogen bonds and close contacts in **(1)**, (a), and **(2)**, (b).[46]

The differences in the molecular interactions outlined above can be seen using Hirshfeld surfaces.[47,48] Figures 8(a-d), and 9(a-b) show the Hirshfeld surfaces and the associated hydrogen bonding and close contacts in **(1)** and **(2)**, with d_{norm} for the opposing aspects of **(1)** and **(2)**. The d_{norm} surfaces highlight contacts that are less than the sum of atomic van der Waals radii (red), longer, (blue) and approximately equal, (white). From Figures 8 and 9, it is clear to see that both the greater number and strengths of the inter- and intramolecular contacts occur in **(2)**. Interestingly, in **(1)**, the shortest and strongest intermolecular contacts involve O(1) and O(2) of the benzothiazinecarboxamide and N(2)-H(2A), while in **(2)** the contacts have effectively been eliminated due to the close packing of the two piroxicam moieties. These have been replaced as the strongest bonding atoms in **(2)**, by O(4) and O(4'), and the two water molecules, one of which O(1W) bridges between **(2a)**, and the second O(2W), that forms a strong bond to a piroxicam molecule in an adjoining unit cell.

Atomic Charges

Atomic charges, evaluated both from monopole populations (Pv) and through integration over atomic basins (Bader charges) (Ω), are reported in Table 6 for selected atoms. As with bond properties, major changes in atomic charge are found across the molecule: S becomes more positive, and O(1) and O(2) more equal, in **(2)** compared to **(1)**. O(3), which is formally a negative enolate in **(2)**, is actually slightly less negative in the zwitterionic form than in **(1)**, while the protonated N(3) is significantly more negative in the zwitterion than it is in the neutral form. Other large changes are seen in O(4), C(2), and all carbons in the pyridine ring. Clearly, these data do not follow the patterns that would be expected on consideration of formal charges and protonation states. To examine these changes in more detail, we have summed individual atomic charges into fragment values for i) pyridine/pyridinium, ii) amide, and iii) benzothiazinecarboxamide fragments. Using the experimental, integrated atomic charge data, these fragments in **(1)** are found to have charges of +0.57, -0.70 and +0.09,

respectively; in **(2)**, these values change to +1.30, -0.62, and -0.66. Thus, proton transfer does indeed lead to a much more positive pyridinium fragment, but this positive charge is delocalised over the entire ring rather than being concentrated on the N—H group. Similarly, the benzothiazinecarboxamide fragment is more negative in the zwitterion, but this is not localised on the enolate group.

Table 6. Atomic charges (*e*) from multipole refinement.

Atom	Pv (*Exp*)	Ω(*Exp*)	Ω(dft)
S(1) **(1)**	0.24	2.92	3.14
(2a)	0.39	2.98	3.19
(2b)	0.48	3.08	3.19
O(1)	-0.39	-1.59	-1.34
	-0.44	-1.45	-1.36
	-0.42	-1.39	-1.37
O(2)	-0.43	-1.40	-1.38
	-0.43	-1.39	-1.38
	-0.49	-1.50	-1.37
O(3)	-0.32	-1.08	-1.18
	-0.34	-0.97	-1.25
	-0.34	-1.06	-1.23
O(4)	-0.34	-1.02	-1.20
	-0.29	-1.16	-1.23
	-0.34	-1.15	-1.23
N(1)	-0.32	-1.21	-1.32
	-0.31	-1.24	-1.33
	-0.31	-1.25	-1.34
N(2)	-0.19	-1.13	-1.28
	-0.20	-1.26	-1.29

	-0.22	-1.26	-1.30
N(3)	-0.11	-0.82	-1.22
	-0.17	-1.27	-1.35
	-0.15	-1.28	-1.35
C(1)	0.00	0.17	0.32
	0.01	0.22	0.28
	0.03	0.25	0.28
C(2)	0.06	0.48	0.63
	0.05	0.82	0.85
	0.00	0.79	0.87
C(3)	0.09	0.09	0.02
	0.04	0.02	0.00
	0.05	0.05	0.00
C(4)	0.09	0.05	0.02
	-0.02	-0.01	-0.02
	-0.03	-0.07	-0.03
C(5)	0.09	0.04	0.01
	0.04	0.05	-0.03
	0.03	0.04	-0.04
C(6)	0.13	0.10	0.01
	-0.01	-0.04	-0.03
	0.08	0.07	-0.04
C(7)	0.03	0.01	0.03
	-0.10	-0.12	-0.02
	0.05	0.05	-0.01
C(8)	-0.04	-0.17	-0.15
	-0.12	-0.27	-0.16
	-0.11	-0.25	-0.15
C(9)	0.17	1.19	1.45

	0.10	1.34	1.39
	0.07	1.25	1.36
C(10)	0.01	0.61	0.94
	0.13	0.91	1.03
	0.14	0.94	1.06
C(11)	0.15	0.15	0.01
	0.02	0.01	-0.01
	0.01	0.02	-0.01
C(12)	-0.06	-0.07	0.01
	0.07	0.10	-0.01
	0.06	0.05	-0.01
C(13)	0.02	-0.07	0.00
	0.07	0.11	-0.01
	0.08	0.10	-0.01
C(14)	0.14	0.56	0.58
	0.04	0.34	0.46
	0.04	0.35	0.46
C(15)	-0.04	0.10	0.40
	-0.27	0.05	0.31
	-0.03	0.15	0.30
H(2)	-0.03	0.26	0.47
	0.25	0.54	0.55
	0.20	0.46	0.56
H(3)	0.14	0.48	0.66
	0.35	0.59	0.55
	0.31	0.59	0.54
H(4)	0.18	0.24	0.05
	0.14	0.15	0.08
	0.10	0.13	0.10

H(5)	0.18	0.25	0.02
	0.06	0.07	0.06
	0.06	0.07	0.05
H(6)	0.08	0.12	0.02
	0.16	0.20	0.06
	0.02	0.05	0.05
H(7)	0.10	0.14	0.06
	0.13	0.14	0.01
	0.09	0.14	0.01
H(11)	-0.03	-0.02	0.08
	0.06	0.07	0.15
	0.04	0.11	0.12
H(12)	0.12	0.14	0.02
	0.08	0.10	0.13
	0.08	0.12	0.01
H(13)	0.07	0.14	0.01
	0.15	0.18	0.09
	0.05	0.09	0.09
H(14)	-0.05	-0.05	0.02
	0.12	0.18	0.12
	0.14	0.19	0.12
H(15A)	0.07	0.04	0.01
	0.08	0.05	0.04
H(15D)	0.03	0.06	0.03
H(15B)	0.16	0.18	0.03
	0.10	0.07	0.07
H(15E)	0.10	0.11	0.08
H(15C)	0.13	0.13	0.01
	-0.00	-0.04	0.01

H(15F)	0.03	0.02	0.04

Table 7 details the atoms with the greatest differences in charge between **(1)** and **(2)**. While no clear trend is observed between the monopole and Bader charges, there are some interesting changes. Considering first the monopole charges, when moving from **(1)** to **(2a)** C(15) becomes slightly more negative, this can be accounted for by C(15) participating in fewer intermolecular contacts in **(2a)**. This effect is also clearly seen in the increased positive charge on C(15) between **(2a)** and **(2b)**. In **(2b)** S(1) becomes slightly more positive, possible due to the fact that O(1) and O(2) are involved in a greater number of intermolecular contacts, increasing the polarisation between the sulfur and oxygen atoms. This is clearly seen in Figure 5(c). Surprisingly, when considering the experimental Bader charges, the largest increase is that of N(3) becoming more negative in both **(2a)** and **(2b)** compared to **(1)**. As has been discussed, what should be a formally positive nitrogen in zwitterionic **(2a,b)**, once again lends support to the delocalisation of the positive charge across the pyridine group. In a similar fashion DFT predicts that in moving to a zwitterionic structure that the enolate carbon C(2) becomes increasingly positively charged, indicating that enolate has little to do with the delocalised negative charge across the benzothiazinecarboxamide.

Table 7. Greatest differences in Atomic charges (*e*), between molecule pairs and the atoms involved.

(**1**) and (**2a**)	ΔPv	-0.23	C(15)
	ΔΩ(*Exp*)	-0.45	N(3)
	Δ(DFT)	+0.22	C(2)
(1) and **(2b)**	ΔPv	+0.24	S(1)

	ΔΩ(*Exp*)	-0.46	N(3)
	ΔΩ(DFT)	+0.24	C(2)
(2a) and **(2b)**	ΔPv	+0.24	C(15)
	ΔΩ(*Exp*)	+0.17	C(7)
	ΔΩ(DFT)	-0.03	C(9)

Electrostatic Potential

The changes in atomic charges found across the molecule are also reflected in the molecular electrostatic potential (MEP) as shown in Figure 10. In the experimental electrostatic potential of **(2)**, the pyridyl nitrogen is more electropositive compared to **(1)**. Similarly, the enolate group is slightly more electropositive in the zwitterion. A strong green colour of the pyridine ring in the zwitterion shows the ring is more electropositive compared to that in **(1)** and this once again suggests the positive charge from the protonation is distributed over the pyridine ring instead of localised on the N—H group. Likewise, the slightly less positive benzothiazinecarboxamide fragment in the zwitterion indicates once again that the negative charge from the proton transfer in the zwitterion is not concentrated on the enolate group. An additional reason for the reduced electron concentration in the benzothiazinecarboxamide fragment may be attributed to the water molecules in **(2)** drawing electrons away from O(4) as can be seen by the highly electropositive region in the hydrogen bond between O(4) and H(1W).

A comparison of the electrostatic potential of the N-methyl and sulfoxide groups in **(1)** and **(2)** show no major differences between them even though the groups in **(2)** are significantly closer to other atoms and thus have a higher potential to form potential bonds. This lack of

change in this group between the two polymorphic forms may be attributed to the inherent stability of these two functional groups and the fact that their relative geometries are almost identical in all three cases. This feature could potentially be utilised in future drug design as potential anchors around which other connections may be formed while they remain constant.

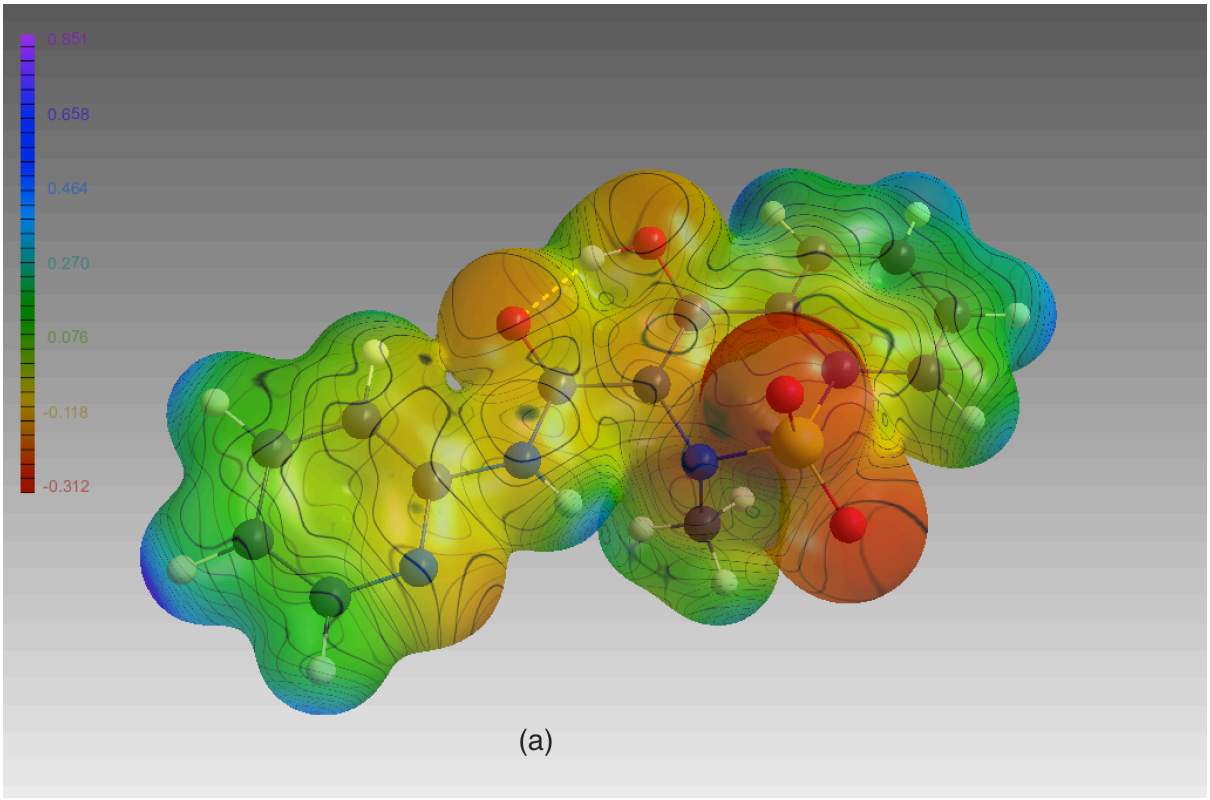

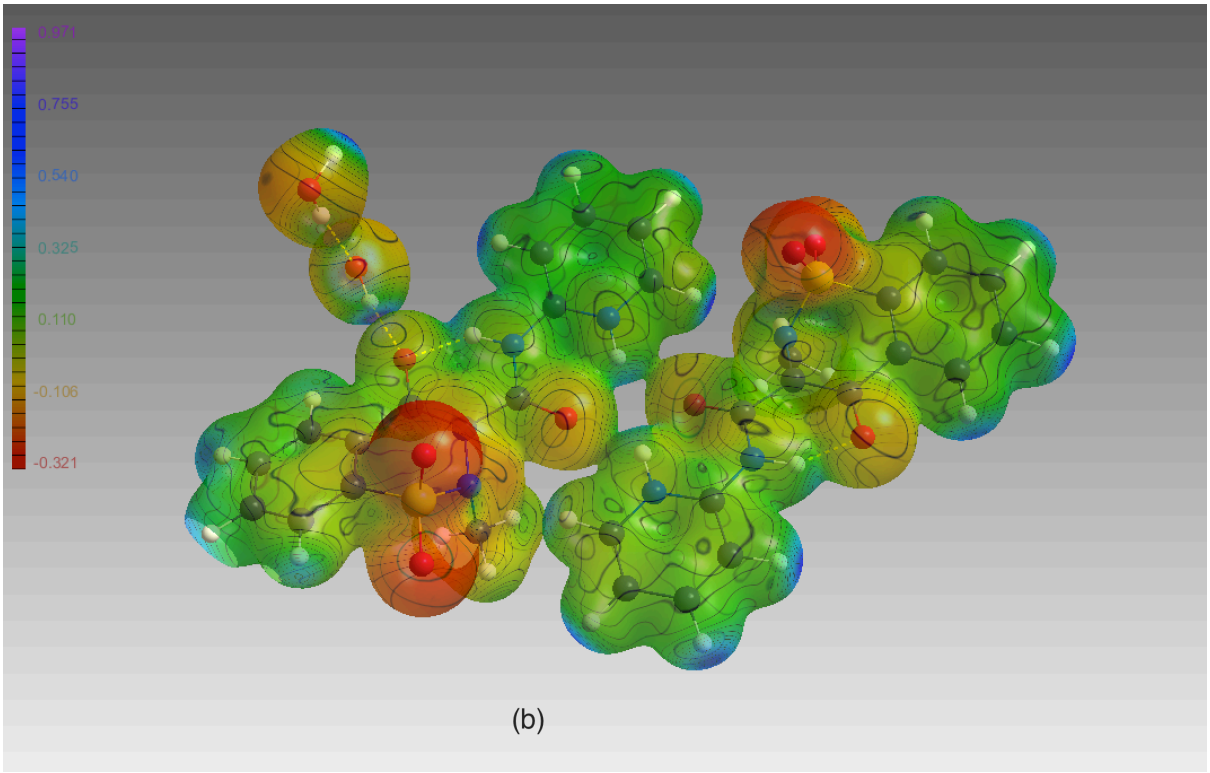

Figure 10. Electrostatic potential of **(1)** (a), and **(2)** (b) plotted on the ρ isosurface[49].

The differences in hydrogen bonding and molecular polarity between forms (**1**) and (**2**) are likely to have a significant effect on pharmaceutically relevant properties such as stability and solubility. Using *ab initio* calculations, it has been noted by Sheth *et al.*[3] that it is the difference in lattice energy and not the conformational energy of individual molecules, (determined to be 0.96 kJ mol^{-1} for each polymorph), that accounts for the observed differences in physical properties. Further, Sheth *et al.*[50] note that the energies of individual molecules in the monohydrate form are 50-58 kJ mol^{-1} greater than in β-piroxicam, which would be expected to destabilise the crystal lattice. To examine this in more detail, lattice energies were calculated for both forms using the LATEN option in XD2006, which is based on total intermolecular interactions energies suggested by Volkov and Coppens.[51] In this manner, we predict the lattice energy for **(1)** to be -304 kJ mol^{-1}, while that for **(2)** is -571 kJ mol^{-1}. The observation that the zwitterionic, monohydrated form of piroxicam has a larger lattice stabilisation (and thus is thermodynamically more stable) is perhaps not a surprise, given the number and strengths of the hydrogen bonding network outlined above. Surprisingly, this can be seen when examining the dipole moment. Sheth *et al.*[50] again report that the gas-phase molecular dipole moment increases when moving from the β-piroxicam structure to the piroxicam monohydrate structure ($\Delta\mu \sim 8$D). Calculation of the in-crystal molecular dipole moment reveals that the β-piroxicam has a dipole moment of 10.14D, while the monohydrate has a marginally smaller MDM of 9.47D. Clearly the water molecules present in the monohydrate lattice stabilise the zwitterion, and therefore lower the free energy of the molecules *via* hydrogen bonding network formation. Accurate quantification of this effect allows a deeper understanding of the physical properties of this drug. Paaver *et al.*[52] reports that form **(1)** displays faster rate of dissolution and greater solubility than **(2)** at

different pHs. This agrees with the lattice energies calculated as lattice energy has a direct correlation to dissolution rate and solubility.

Conclusion

In this study we demonstrated the differences between β-piroxicam and piroxicam monohydrate by carrying out experimental charge density studies. The presence of water molecules in piroxicam monohydrate crystal results in the formation of a zwitterionic structure with a concomitant rotation of the pyridine ring, resulting in the formation of a number of strong hydrogen bonds that aids the stabilisation of this crystal. Lower solubility and higher stability of the monohydrate polymorph are explained by a larger numbers of, and stronger interactions inside the crystal. Key to this stabilisation is water molecules, their ability to stabilise the zwitterionic piroxicam leads to a higher lattice energy compared to β-piroxicam. Furthermore, electrostatic potential of the zwitterionic monohydrate has also demonstrated the charges caused by proton transfer are not localised and concentrated on the atoms involved but are spread and re-distributed across different sections of the piroxicam molecule, suggesting chemistry might be different to what we assumed previously. The study of polymorphism in piroxicam provides us knowledge on the behaviour of zwitterionic molecules and therefore gives us potential insights into new methods available which may benefit efforts in crystal engineering.

Acknowledgements
DEH would like to thank The University of Sydney Bridging Support Scheme for funding. The work was supported by the Danish National Research Foundation (Center for Materials Crystallography, DNRF-93)

References

1. Thayer, A. M., Form and function. *Chem. Eng. News* **2007,** *85*, 17-30.
2. Mihalic, M.; Hofman, H.; Kajfez, F.; Kuftinec, J.; Blazevic, N.; Zinic, M., Physicochemical and analytical characteristics of piroxicam. *Acta Pharmaceutica Jugoslavica* **1982,** *32* (1), 13-20.
3. Sheth, A. R.; Bates, S.; Muller, F. X.; Grant, D. J., Polymorphism in piroxicam. *Crystal growth & design* **2004,** *4* (6), 1091-1098.
4. Vrečer, F.; Vrbinc, M.; Meden, A., Characterization of piroxicam crystal modifications. *International journal of pharmaceutics* **2003,** *256* (1), 3-15.
5. Upadhyay, P. P.; Bond, A. D., Crystallization and disorder of the polytypic α 1 and α 2 polymorphs of piroxicam. *CrystEngComm* **2015**.
6. FDA, Guidance for Industry ANDAs: Pharmaceutical Solid Polymorphism **2007**.
7. Bordner, J.; Richards, J. A.; Weeks, P.; Whipple, E. B., Piroxicam* Monohydrate: a Zwitterionic Form, C15H13N304S.H20. *Acta Crystallogr., Sect. C* **1984,** (40), 989-990.
8. Bader, R. F. W., Atoms in molecules: a quantum theory. *Clarendon Press: Oxford ; New York* **1990**.
9. Abramov, Y. A., On the possibility of kinetic energy density evaluation from the experimental electron-density distribution. *Acta Crystallogr., Sect. A: Found. Crystallogr.* **1997,** *A53* (3), 264-272.
10. Hoser, A. A.; Jarzembska, K. N.; Dobrzycki, L.; Gutmann, M. J.; Wozniak, K., Differences in Charge Density Distribution and Stability of Two Polymorphs of Benzidine Dihydrochloride *Crystal growth & design* **2012,** *12*, 3526 - 3539.
11. Overgaard, J.; Hibbs, D. E., The experimental electron density in polymorphs A and B of the anti-ulcer drug famotidine. *Acta Crystallogr., Sect. A* **2004,** *A60*, 480-487.
12. Sovago, I.; Gutmann, M. J.; Hill, J. G.; Senn, H. M.; Thomas, L. H.; Wilson, C. C.; Farrugia, L. J., Experimental Electron Density and Neutron Diffraction Studies on the Polymorphs of Sulfathiazole. *Crystal growth & design* **2014,** *14*, 1227-1239.
13. Oxford, D. *CrysAlis*^{Pro}, 1.171.37.31b; Oxford Diffraction Ltd: Abingdon, England, 2006.
14. Sheldrick, G. M., A short history of SHELX. *Acta Crystallogr., Sect. A: Found. Crystallogr.* **2008,** *64* (1), 112-122.
15. Sheldrick, G. M., Crystal structure refinement with SHELXL. *Acta Crystallogr., Sect. C: Cryst. Struct. Commun.* **2015,** *71* (1), 3-8.
16. Allen, F. H.; Kennard, O.; Watson, D. G.; Brammer, L.; Orpen, A. G.; Taylor, R., Tables of bond lengths determined by x-ray and neutron diffraction. Part 1. Bond lengths in organic compounds. *J. Chem. Soc., Perkin Trans. 2* **1987,** (12), S1-S19.
17. Zeidler, A.; Salmon, P. S.; Fischer, H. E.; Neuefeind, J. C.; Simonson, J. M.; Markland, T. E., Isotope effects in water as investigated by neutron diffraction and path integral molecular dynamics. *Journal of Physics: Condensed Matter* **2012,** *24* (28), 284126.
18. Volkov, A.; Macchi, P.; Farrugia, L. J.; Gatti, C.; Mallinson, P.; Richter, T.; Koritsanszky, T. *XD2006- a computer program for multipole refinement, topological analysis of charge densities and evaluation of intermolecular energies from experimental or theoretical structure factors*, 2006.
19. Hansen, N. K.; Coppens, P., Electron population analysis of accurate diffraction data. VI. Testing aspherical atom refinements on small-molecule data sets. *Acta Crystallogr., Sect. A* **1978,** *A34* (6), 909-21.
20. (a) Hibbs, D. E.; Austin-Woods, C. J.; Platts, J. A.; Overgaard, J.; Turner, P., Experimental and theoretical charge density study of the neurotransmitter taurine. *Chem. - Eur. J.* **2003,** *9* (5), 1075-1084; (b) Hibbs, D. E.; Hanrahan, J. R.; Hursthouse, M. B.; Knight, D. W.; Overgaard, J.; Turner, P.; Piltz, R. O.; Waller, M. P., Experimental and theoretical charge distribution in (Z)-N-methyl-C-phenylnitrone. *Org. Biomol. Chem.* **2003,** *1* (6), 1034-1040.
21. Schmokel, M. S.; Cenedese, S.; Overgaard, J.; Jorgensen, M. R. V.; Chen, Y. S.; Gatti, C.; Stalke, D.; Iversen, B. B., *Inorganic Chemistry* **2012,** *51*, 8607-8616.
22. Du, J. J.; Overgaard, J.; Williams, P. A.; Platts, J. A.; Hibbs, D. E., *in preparation.*

23. Clementi, E.; Raimondi, D. L., Atomic Screening Constants from SCF Functions. *The Journal of Chemical Physics 38*, 2686-2689.
24. Hirshfeld, F. L., Can x-ray data distinguish bonding effects from vibrational smearing? *Acta Crystallogr., Sect. A* **1976,** *A32, Pt. 2*, 239-44.
25. Hoser, A. A.; Dominiak, P. M.; Wozniak, K., Towards the best model for H atoms in experimental charge-density refinement. *Acta Crystallogr., Sect. A: Found. Crystallogr.* **2009,** *65* (4), 300-311.
26. (a) Spackman, M. A., Molecular electric moments from x-ray diffraction data. *Chem. Rev.* **1992,** *92* (8), 1769-97; (b) Spackman, M. A., Hydrogen bond energetics from topological analysis of experimental electron densities: Recognising the importance of the promolecule. *Chem. Phys. Lett.* **1999,** *301* (5,6), 425-429; (c) Spackman, M. A.; Byrom, P. G.; Alfredsson, M.; Hermansson, K., Influence of intermolecular interactions on multipole-refined electron densities. *Acta Crystallogr., Sect. A: Found. Crystallogr.* **1999,** *A55* (1), 30-47.
27. Koritsanszky, T. S.; Coppens, P., Chemical applications of x-ray charge-density analysis. *Chem. Rev. (Washington, D. C.)* **2001,** *101* (6), 1583-1627.
28. Madsen, A. O.; Sorensen, H. O.; Flensburg, C.; Stewart, R. F.; Larsen, S., Modeling of the nuclear parameters for H atoms in X-ray charge-density studies. *Acta Crystallogr., Sect. A: Found. Crystallogr.* **2004,** *A60* (6), 550-561.
29. Madsen, A. O., SHADE web server for estimation of hydrogen anisotropic displacement parameters. *J. Appl. Crystallogr.* **2006,** *39* (5), 757-758.
30. Nguyen, T. H.; Groundwater, P. W.; Platts, J. A.; Hibbs, D. E., Experimental and Theoretical Charge Density Studies of 8-Hydroxyquinoline Cocrystallized with Salicylic Acid. *J. Phys. Chem. A* **2012,** *116* (13), 3420-3427.
31. Du, J. J.; Váradi, L.; Tan, J.; Zhao, Y.; Groundwater, P. W.; Platts, J. A.; Hibbs, D. E., Experimental and Theoretical Charge Density Distribution in Pigment Yellow 101 *Physical Chemistry and Chemical Physics* **2015,** *17*, 4677-4686.
32. Frisch, M. J.; Trucks, G. W.; Schlegel, H. B.; Scuseria, G. E.; Robb, M. A.; Cheeseman, J. R.; Scalmani, G.; Barone, V.; Mennucci, B.; Petersson, G. A.; Nakatsuji, H.; Caricato, M.; Li, X.; Hratchian, H. P.; Izmaylov, A. F.; Bloino, J.; Zheng, G.; Sonnenberg, J. L.; Hada, M.; Ehara, M.; Toyota, K.; Fukuda, R.; Hasegawa, J.; Ishida, M.; Nakajima, T.; Honda, Y.; Kitao, O.; Nakai, H.; Vreven, T.; Montgomery, J. A., Jr.; Peralta, J. E.; Ogliaro, F.; Bearpark, M.; Heyd, J. J.; Brothers, E.; Kudin, K. N.; Staroverov, V. N.; Kobayashi, R.; Normand, J.; Raghavachari, K.; Rendell, A.; Burant, J. C.; Iyengar, S. S.; Tomasi, J.; Cossi, M.; Rega, N.; Millam, N. J.; Klene, M.; Knox, J. E.; Cross, J. B.; Bakken, V.; Adamo, C.; Jaramillo, J.; Gomperts, R.; Stratmann, R. E.; Yazyev, O.; Austin, A. J.; Cammi, R.; Pomelli, C.; Ochterski, J. W.; Martin, R. L.; Morokuma, K.; Zakrzewski, V. G.; Voth, G. A.; Salvador, P.; Dannenberg, J. J.; Dapprich, S.; Daniels, A. D.; Farkas, Ö.; Foresman, J. B.; Ortiz, J. V.; Cioslowski, J.; Fox, D. J. *Gaussian09*, 2006.
33. Becke, A. D., A new mixing of Hartree-Fock and local-density-functional theories. *J. Chem. Phys.* **1993,** *98* (2), 1372-7.
34. Lee, C.; Yang, W.; Parr, R. G., Development of the Colle-Salvetti correlation-energy formula into a functional of the electron density. *Phys. Rev. B: Condens. Matter* **1988,** *37* (2), 785-9.
35. Yannai, T.; Tew, D. P.; Handy, N. C., A new hybrid exchange-correlation functional using the Coulomb-attenuating method (CAM-B3LYP). *Chem. Phys. Lett.* **2004,** *393* (1), 51-57.
36. Keith, T. A. *AIMAll*, 14.06.21; TK Gristmill Software: Overland Park KS, USA, 2014.
37. Farrugia, L. J., ORTEP-3 for windows - a version of ORTEP-III with a graphical user interface (GUI). *J. Appl. Crystallogr.* **1997,** *30* (5, Pt. 1), 565.
38. Kojic-Prodic, B.; Ruzic-Toros, Z., Structure of the antiinflammatory drug 4-hydroxy-2-methyl-N-2-pyridyl-2H-1λ6,2-benzothiazine-3-carboxamide 1,1-dioxide (piroxicam). *Acta Crystallogr., Sect. B* **1982,** *B38* (11), 2948-51.
39. Firme, C. L.; Antunes, O. A. C.; Esteves, P. M., Relation between bond order and delocalization index of QTAIM. *Chemical Physics Letters* **2009,** *468* (4–6), 129-133.

40. Coppens, P., *X-Ray Charge Densities and Chemical Bonding* Oxford University Press New York, 1997.
41. Du, J. J.; Váradi, L.; Tan, J.; Zhao, Y.; Groundwater, P. W.; Platts, J. A.; Hibbs, D. E., Experimental and Theoretical Charge Density Distribution in Pigment Yellow 101 (*in press*). *Physical Chemistry and Chemical Physics* **2015**.
42. Espinosa, E.; Molins, E.; Lecomte, C., Hydrogen bond strengths revealed by topological analyses of experimentally observed electron densities. *Chem. Phys. Lett.* **1998,** *285* (3,4), 170-173.
43. Steiner, T., The Hydrogen Bond in the Solid State. *Angew. Chem., Int. Ed.,* **2002,** *41* (1), 48-76.
44. Gavezzotti, A., Non-conventional bonding between organic molecules. The 'halogen bond' in crystalline systems. *Mol. Phys.* **2008,** *106* (12-13), 1473-1485.
45. Spackman, M. A., How Reliable Are Intermolecular Interaction Energies Estimated from Topological Analysis of Experimental Electron Densities? *Crystal Growth & Design* **2015,** *15* (11), 5624-5628.
46. Macrae, C. F.; Bruno, I. J.; Chisholm, J. A.; Edgington, P. R.; McCabe, P.; Pidcock, E.; Rodriguez-Monge, L.; Taylor, R.; Streek, J. v. d.; Wood, P. A., Mercury CSD 2.0 - new features for the visualization and investigation of crystal structures. *J. Appl. Crystallogr.* **2008,** *41*, 466-470.
47. McKinnon, J. J.; Spackman, M. A.; Mitchell, A. S., Novel tools for visualising and exploring intermolecular interactions in molecular crystals. *Acta Crystallogr., Sect. B* **2004,** *60*, 627-668.
48. Spackman, M. A.; Jayatilaka, D., Hirshfeld surface analysis. *CrystEngComm* **2009,** *11*, 19-32.
49. Hubschle, C. B.; Luger, P., MolIso - a program for colour-mapped iso-surfaces. *J. Appl. Crystallogr.* **2006,** *39*, 901-904.
50. Sheth, A. R.; Zhou, D.; Muller, F. X.; Grant, D. J. W., Dehydration Kinetics of Piroxicam Monohydrate and Relationship to Lattice Energy and Structure. *Journal of Pharmaceutical Sciences* **2004,** *93* (12), 3013-3026.

51. (a) Volkov, A.; Koritsanszky, T.; Coppens, P., Combination of the exact potential and multipole methods (EP/MM) for evaluation of intermolecular electrostatic interaction energies with pseudoatom representations of molecular electron densities. *Chem. Phys. Lett.* **2004,** *391*, 170-175; (b) Volkov, A.; Li, X.; Koritsanszky, T.; Coppens, P., Ab Initio quality electrostatic atomic and molecular properties including intermolecular energies from a transferable theoretical pseudoatom databank,. *Journal of Physical Chemistry A.* **2004,** *A108*, 4283-4300; (c) Volkov, A.; P. Coppens, J. C. C., 25, 921-934 (2004), Calculation of electrostatic interaction energies in molecular dimers from atomic multipole moments obtained by different methods of electron density partitioning. *J. Comput. Chem.* **2004,** *25*, 921-934.

52. Paaver, U.; Lust, A.; Mirza, S.; Rantanen, J.; Veski, P.; Heinämäki, J.; Kogermann, K., Insight into the solubility and dissolution behavior of piroxicam anhydrate and

monohydrate forms. *International journal of pharmaceutics* **2012,** *431*, 111-119.